

Soft Matter

Accepted Manuscript



This is an *Accepted Manuscript*, which has been through the Royal Society of Chemistry peer review process and has been accepted for publication.

Accepted Manuscripts are published online shortly after acceptance, before technical editing, formatting and proof reading. Using this free service, authors can make their results available to the community, in citable form, before we publish the edited article. We will replace this *Accepted Manuscript* with the edited and formatted *Advance Article* as soon as it is available.

You can find more information about *Accepted Manuscripts* in the [Information for Authors](#).

Please note that technical editing may introduce minor changes to the text and/or graphics, which may alter content. The journal's standard [Terms & Conditions](#) and the [Ethical guidelines](#) still apply. In no event shall the Royal Society of Chemistry be held responsible for any errors or omissions in this *Accepted Manuscript* or any consequences arising from the use of any information it contains.

Tubular growth and bead formation in the lyotropic lamellar phase of a lipid

Tripta Bhatia,^{*a,b} Yashodhan Hatwalne,^a and N. V. Madhusudana^a

Received Xth XXXXXXXXXXXX 20XX, Accepted Xth XXXXXXXXXXXX 20XX

First published on the web Xth XXXXXXXXXXXX 200X

DOI: 10.1039/b000000x

We use fluorescent confocal polarised microscopy (FCPM) to study tubular growth upon hydration of dry DOPC (1,2-dioleoyl-sn-glycero-3-phosphocholine) in water or water-glycerol mixtures. We have developed a model to relate the FCPM intensity profiles to the multilamellar structures of the tubules. Insertion of an additional patch inside a tubule produces a beaded structure, while a straight configuration is retained if the growth is on the outside. We use a simple model to argue that a reduction in overall curvature energy drives bead formation.

1 Introduction

Virchow reported the observations of tubular structures that form on adding water to the lipid extracts obtained from various organs, back in 1854. He named these structures “myelins”¹. More than 100 years later, in 1966, Chapman and Fluck observed similar structures when the *synthetic* phospholipid dipalmitoyl phosphatidylcholine (DPPC) is hydrated above the chain melting transition temperature^{2,3}, indicating that a necessary condition for myelin figures (MFs) during or upon hydration is the non-crystalline, fluid phase of the amphiphilic lipids. Subsequent observations under a scanning electron microscope equipped with a cryo-stage revealed that these tubules are multi-lamellar, with a central core filled with the solvent⁴. In the more recent contact experiments reported by Zou and Nagel⁵, myelins were produced by hydrating *previously humidified, fully swollen* surfactant plaques. In another experiment, they showed that puncturing the fully swollen lamellar stacks in excess water leads to tubules growth from the punctured site. They reconcile these observations by suggesting that myelin figures are non-equilibrium structures forming only in the presence of a net driving force, such as that provided by hydration differential. Zou has proposed a microscopic theory in which myelin growth is attributed to surfactant flow at the surfactant/water interface⁶ in presence of a hydration stress. Following the reverse, dehydration experiment, Huang *et al.*⁷ have proposed a slightly different model for myelin (hereafter called tubule) formation from a multilamellar disk upon evaporation of the solvent. In this model, a reduced bilayer repeat spacing (due to dehydration) increases the bilayer repulsion. If flat bilayers transform into cylinders,

bilayer repeat spacing increases, keeping the total area and the lamellar volume constant. Assuming the core radius of tubules to be half the layer spacing, they find that the decrease in inter-bilayer repulsion through the topological lamellar-to-tubular transition more than compensates for additional curvature energy of the incipient tubules.

Here we describe the experiments in which a nominally *dry* pool of a fluid-phase lipid DOPC reservoir undergoes swelling by capillary action. We find that an abrupt “burst” event characterised by rapid appearance of microscopic initial tubules locally triggers the formation of long-lived additional new multilamellar tubules. In these post-burst, long-lived tubules an unusual complex topography appears reproducibly. Specifically, we observe localised bulging of some tubules (bead formation) in which additional lamellar inclusions are found within the tubule interior. We also observe tubules with exterior lamellar attachments which do not lead to the formation of beads. We propose a simple phenomenological model for the structure and stability of bead-encapsulating myelin tubules. This paper is organised as follows: The description of experimental methods is followed by a summary of observations. The modelling and analysis essential for extracting structural information from FCPM images is discussed in the next two sections. This is followed by the description of structural details of observed, representative morphologies. The phenomenological model for the structure and stability of beads is discussed in the last section.

Structurally analogous multilamellar tubules, also known as MFs are also seen in biological systems; a prominent example being myelin figures in pulmonary lining⁸, an extra-cellular lipid-protein coat at the lung alveolar surface. The composition and the conditions under which MFs are found in biological systems differ from those of multilamellar tubules discussed in this paper. However, the structural aspects as well as physi-

^a Raman Research Institute, C. V. Raman Avenue, Bangalore 560080, India.

^b Present address: Department of Physics, Chemistry and Pharmacy, University of Southern Denmark, Odense, Denmark; E-mail: bhatia@sdu.dk

cal processes (such as the mechanism of bead formation) discussed here may be of relevance in biological contexts. Membrane tubules are also being explored for applications such as templates for nanofluidic conduits and networks⁹, and as deformable containers for the study of biochemical reactions in nanoscale confinement¹⁰. Controlled introduction of beaded protrusions in multilamellar tubules may have practical use in such applications.

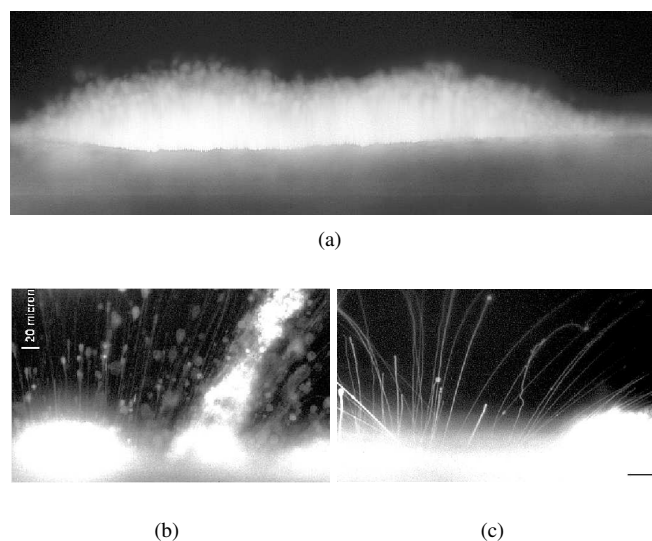


Fig. 1 Epi-fluorescence images: (a) Before burst. (b) The burst, about 22 minutes after adding water. (c) About 20 minutes post-burst. Scale bar 20 μm .

2 Experimental methods

We prepare stock solutions of the lipid DOPC (purchased from Sigma) and the membrane dye, lissamine rhodamine B 1,2-dihexadecanoyl-sn-glycero-3-phosphoethanolamine, triethylammonium salt (rhodamine DHPE, purchased from Molecular Probes) in chloroform. Dye solution is added to lipid stock (2 mg/ml) such that dye concentration is about 0.002 mole per mole of lipid. In the lamellar phase, dye molecules are known to be incorporated in lipid bilayers¹¹. Sample cells are prepared which consist of a glass coverslip onto which about 20–50 μl of lipid solution is pipetted at the center (using a Hamilton syringe). Sample-cells are gently dried under a nitrogen stream and kept covered inside a desiccator overnight. For some experiments, coverslips were spin-coated at 4000 rpm with the same lipid sample. Coated coverslip with dried sample was glued to a larger coverslip at the edges using spacers of about 100 μm thickness. Solvent was introduced between coverslips of sample cells by capillary action. For some experiments the open edges were sealed using silicone glue, im-

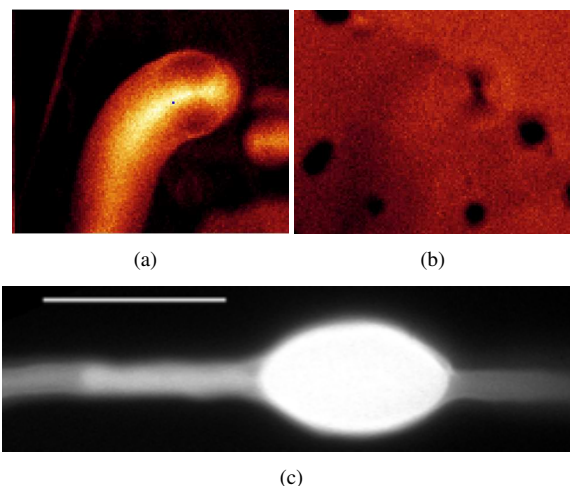


Fig. 2 (a) FCPM image (30 $\mu\text{m} \times 38 \mu\text{m}$) of a tubule growing from the reservoir. (b) The same region at a lower value of z , showing defects at the tubule base. (c) Epi-fluorescence image of a bulged portion or “bead” on a tubule, showing multilamellar morphology, with additional layers inside the main tubule, scale bar 20 μm .

mediately after the solvent filled the whole gap (sealed sample cells). We have used the following solvents: water (refractive index (RI) 1.33), water-glycerol 80-20 v/v (RI 1.357) and water-glycerol 10-90 v/v (RI 1.469). The ordinary RI n^o of neat DOPC¹² is about 1.46. We calculate the ordinary RI (n_L^o) in the lamellar phase (solvent of RI n^s) using $n_L^o = n^o \phi_l + n^s \phi_s$ where ϕ_l and ϕ_s are respectively the volume fractions of DOPC and solvent¹². The birefringence in the lamellar phase of DOPC (20 wt %) in a glycerol-water (91:9 % w/w) mixture (295 K, 589 nm wavelength)¹³ is about 0.026. Sample cells are observed under Epi-fluorescence microscope (Zeiss) and an FCPM (LEICA TCS-SP2, He-Ne laser (543 nm) source) equipped with a 40x dry objective (0.85 N.A.) having a correction collar. We take multiple confocal z -slices of each tubule, from bottom to top of each tubule and select the xy -scan corresponding to the largest horizontal ($z = 0$) cross-section, and average over the repeated scans of this cross-section, for analysis. The epi-fluorescence microscope is equipped with an EMCCD-camera (Cascade 650, Photonics) and a mercury-lamp.

3 Summary of observations

In unsealed *syringe-coated* sample cells, dried lipid on the substrate swells upon adding water, resulting in the nucleation of multilamellar structures (fig. 1a) as can be seen coming out from the lipid-reservoir. After about 20-40 minutes of swelling, a sudden and dramatic instability event (burst) is observed where the pre-existing lipid structures are co-

operatively pushed away from the lipid-reservoir into the solvent leaving behind tethers (thin lipid tubes) as connections to the lipid reservoir (fig. 1b). The thin tubes retract into the reservoir. From the same region (where the burst has occurred), the nucleation and growth of tubules of diameter in the range of a few μm (fig. 1c) are observed. We have also observed fast-retraction and bulging of tubules, growth of branched tubular structures *etc.* The growth and retraction rates of these new tubules is found to be linear and vary from 1 to 40 $\mu\text{m/s}$. Tubules retract as the solvent starts to evaporate. Upon adding the water again swelling and growth of tubules is observed, but we do not observe the burst event. We slow down the growth of tubules by using glycerol-water mixture as solvent. In this case we do not observe the burst, although tubules grow and remain stable until the solvent starts to evaporate, in about half a day.

We found that in the *sealed* sample cells, the tubules remain stable for a couple of days and thereafter undergo a series of morphological transitions. A uniform cylindrically shaped single core tubule after 2 days becomes a complex multi-lamellar tube with multiply connected cores and later dissolves completely into the solvent.

FCPM images show that tubules originate from *defects* which appear to be holes or edges in the lipid reservoir (fig. 2a,b). This is further supported by the observation that tubules do not grow upon adding water in unsealed *spin-coated* samples. The ‘‘puncturing experiment’’ reported previously⁵ is also in agreement with our observations. Epifluorescence observations clearly show that tubules with uniform cross-section often acquire additional layers as inclusions in the core and develop a bulge (bead) (fig. 2c). Typically, beads appear near the reservoir and move away as tubules grow. Confocal scans at the largest cross-section of two beads shown in figs. 3(a), 4(a) clearly reveal the *inclusion* of additional lamellar patches within the tubule interior. Tubules with additional lamellar patches attached to the *exterior* (fig. 5(a)) do not form beads.

4 Modelling tubules for FCPM

We model tubules as cylindrically symmetric structures with fixed lamellar spacing. Dye molecules orient with their long axes along \hat{r} of the cylindrical polar coordinate system (r, η, x) , with polar angle η defined in the yz -plane (fig. 6). The absorption transition dipole moment of dye molecules \hat{d}_a lies in the bilayer plane¹¹, orthogonal to \hat{r} . Excited dye molecules emit fluorescence radiation isotropically. The detected fluorescence intensity $I_D(x, y = y_1)$ has contributions from all the *differently oriented dye molecules* within the confocal slice thickness Δ_z at $y = y_1$. The image is formed by rays entering the objective after taking distinct paths within the sample cell. We therefore need to (i) average over all

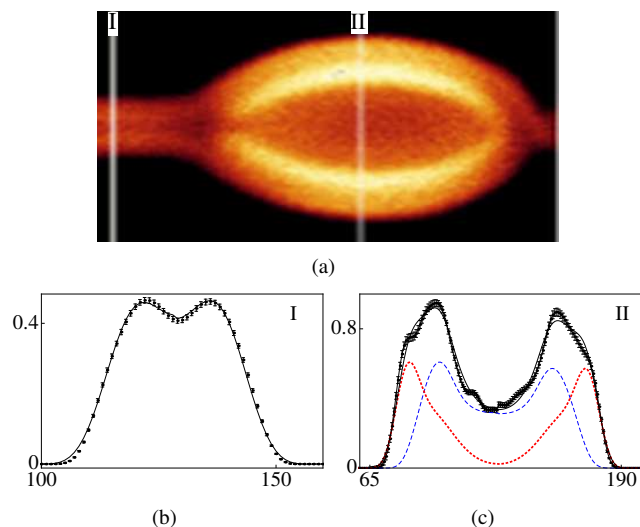


Fig. 3 (a) FCPM image of a bead on a tubule (polarisation along the tubule axis), 80-20 v/v water-glycerol solvent. (b, c): Intensity profiles (arbitrary units, plotted against pixel number). (b) Cross-section I: experimental (with error bars), model (smooth curve) $(r_c, r_o) = (0.4, 0.8)\mu\text{m}$, $\alpha = 0.46$. (c) Cross-section II: bead composed of two tubules, experimental (with error bars), model (black curve), constituent tubules (dotted and dashed curves), $((r_{c1}, r_{o1}), (r_{c2}, r_{o2})) = ((1.2, 2.1), (2.1, 2.4))\mu\text{m}$, $\alpha = 0.6$.

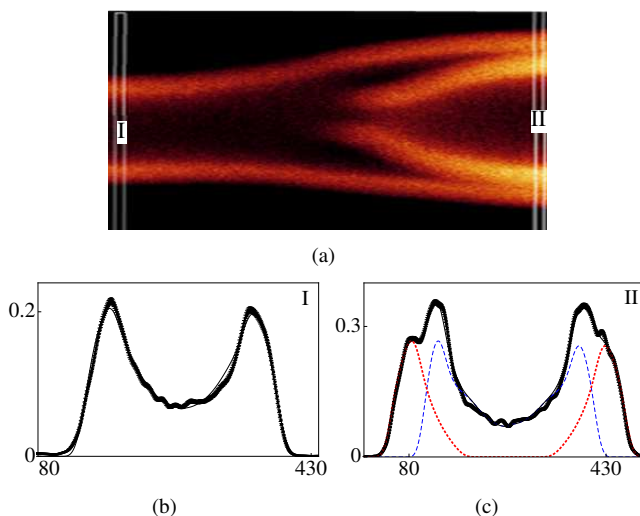


Fig. 4 (a) FCPM image of a beaded tubule with a much larger diameter as compared to the one shown in fig. 4(a). 10-90 v/v water-glycerol solvent. (b) Cross-section I: $(r_c, r_o) = (2.1, 3.1)\mu\text{m}$, $\alpha = 0.2$. (c) Cross-section II: $((r_{c1}, r_{o1}), (r_{c2}, r_{o2})) = ((2.8, 3.6), (3.8, 5.0))\mu\text{m}$, $\alpha = 0.26$, we follow the convention used in fig.(3(b),(c)) to represent experimental and model curves.

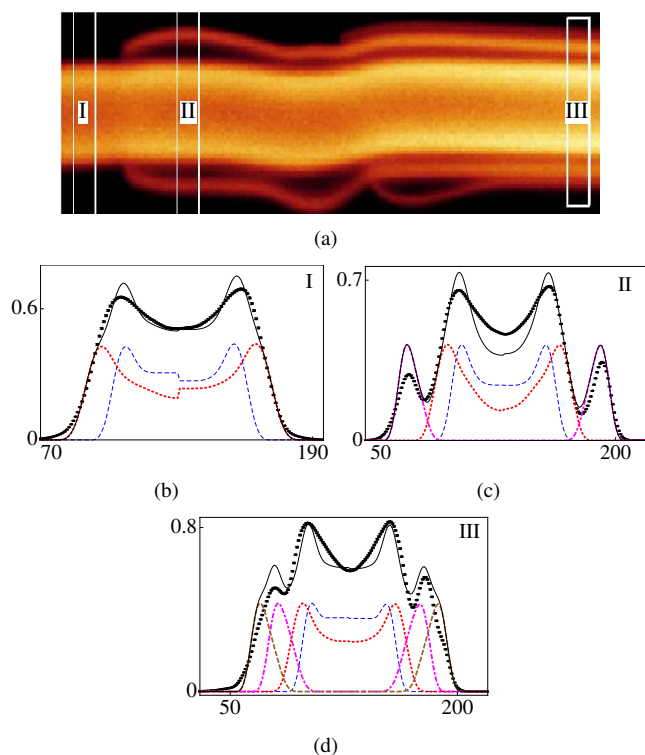


Fig. 5 (a) FCPM image of a tubule with additional exterior patches burrowing into it, 10-90 v/v water-glycerol solvent.

(b) $((r_{c1}, r_{o1}), (r_{c2}, r_{o2})) = ((1.5, 1.6), (1.8, 2.4)) \mu\text{m}$, $\alpha = 0.43$, (c) $((r_{c1}, r_{o1}), (r_{c2}, r_{o2}), (r_{c3}, r_{o3})) = ((1.5, 1.8), (1.8, 2.5), (3.4, 3.5)) \mu\text{m}$, (d) $((r_{c1}, r_{o1}), (r_{c2}, r_{o2}), (r_{c3}, r_{o3}), (r_{c4}, r_{o4})) = ((1.5, 1.6), (1.6, 2.2), (2.7, 3.0), (3.2, 3.4)) \mu\text{m}$, $\alpha = 0.43$. In (b), (c) and (d), $\alpha = 0.42$.

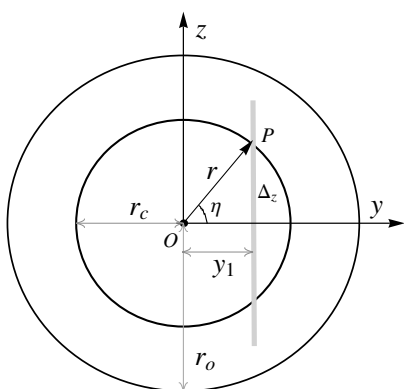


Fig. 6 Transverse cross-section of a uniform cylindrical tubule, core and outer radii r_c and r_o respectively. Δ_z (shown in grey) is the confocal slice thickness.

possible orientations of the dye molecules, and (ii) trace the path of rays entering the objective, for all points (such as P (fig. 6)) within the confocal slice. The electric field \hat{E}_i of the incident linearly polarised laser beam makes an angle ψ with the x -axis. The probability of photon absorption (and therefore, emission) by a dye molecule at the point P($r, \eta, x = 0$) is $P_a(\eta, \psi) \propto I_0 \langle (\hat{d}_a \cdot \hat{E}_i)^2 \rangle \propto I_0 F(\eta, \psi)$, where I_0 is the intensity of the incident laser beam, angular brackets denote average over all possible orientations of \hat{d}_a in the bilayer plane, and $F(\eta, \psi) = (9 - 3 \cos 2\eta + 6 \cos^2 \eta \cos 2\psi)/24$.

We trace the rays by taking into account the refractive indices of the coverslip, solvent and the lamellar structure; the contributions from the total internal reflection at the lamella-solvent interfaces, and the numerical aperture of the objective are also included in the calculation. We evaluate $P_a(\eta, \psi)$ numerically, and have written a computer code for ray-tracing to obtain the model intensity profile $I_M(x, y; r_c, r_o, \Delta_z)$, with inner radius r_c , outer radius r_o , and Δ_z as fitting parameters (see the next section). Note that the objective used has a correction collar, the images analysed are obtained at the widest part of the tubule, and the slice thickness Δ_z is used as a fitting parameter, thus obviating the need for corrections due to spherical aberration.

5 Image processing and fitting

We oversample $I_D(x, y)$ at an adequately high spatial frequency, and enhance the signal-to-noise ratio (SNR) by processing it through a suitable low-pass filter to obtain the smoothed profile $I_{sm}(x, y)$. In Fourier domain the width of the low-pass filter is given by $m_q = (N \times \text{pixel width})/R$, where R is the spatial scale in the image domain over which we want to reduce the noise, and N is the size of the image in pixels. We vary R up to the point spread function-width, and find the corresponding SNR for $I_{sm}(x, y)$. The SNR has a maximum at the ‘‘smoothing radius’’, r_{opt} . In order to ensure that spatial variations on the scale of interest are not significantly affected, we use a filter with the conservative smoothing radius¹⁴ $r_s = r_{opt}/2$.

Recall that we analyse confocal images having the widest horizontal cross-section (see Section 2) of the lipid structures. For beads, $I_D(x, y)$ shows a noticeable deviation from cylindrical symmetry (fig. 3c), (fig. 4c). We locate the centre of a given cross-section by maximising the intensity cross-correlation function. We model the two halves (divided by the xz -plane) separately to estimate the fitting parameters (r_c, r_o, Δ_z) , use these as seed values, and fit $I_M(x, y; r_c, r_o, \Delta_z)$ for each half to $I_{sm}(x, y)$ by using appropriate intensity scaling factor

$$\alpha(x) = \frac{\sum_{j=1}^N I_{sm}(x, y_j) I_M(x, y_j; r_c, r_o, \Delta_z)}{\sum_{j=1}^N I_M^2(x, y_j; r_c, r_o, \Delta_z)}, \quad (1)$$

where y_j denotes the pixel number along the y -axis. $\alpha(x)$ denotes a common intensity scaling factor for the overall model intensity profile of the tubule (or bead). In Eqn. (1), a higher value of α required for the fit of I_{sm} with I_M reflects a lower number density of the dye molecules present in the tubule, and vice-versa. Previous studies have reported that the dye is homogeneously distributed in the fluid phase of a membrane and does not aggregate at such a low concentration¹¹. However, we have found that a slightly lower value of α is required for the straight part of the tube compared to the bend part of the same tube (fig. 3c), (fig. 4c), as discussed in the section below.

For a given cross-section at x , the best fits are obtained by minimising the weighted $\chi^2(\alpha, r_c, r_o, \Delta_z)$ given by¹⁵

$$\chi^2 = \frac{1}{N} \sum_{j=1}^N \left[(I_{sm}(y_j) - \alpha \sum_k I_M^{(k)}(y_j; r_c, r_o, \Delta_z)) / \sigma_j \right]^2, \quad (2)$$

where σ_j is the standard deviation of the noise associated with j^{th} pixel along the y -axis for a given x , and k labels separate concentric tubules in a given cross-section.

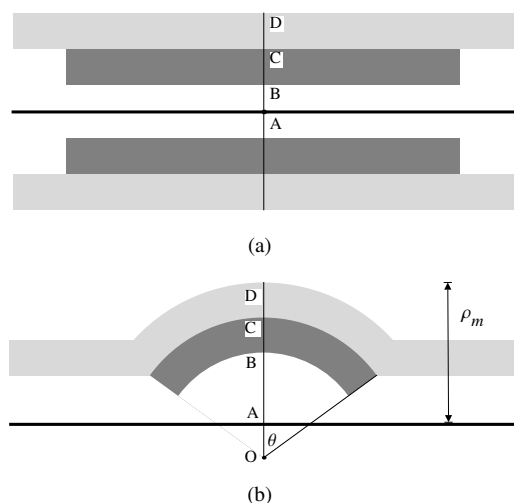


Fig. 7 (a) Schematics of axial cross-section of a tubule with the dark region representing a stitched scroll that fits snugly into the outer tubule. Outer radius $AD = r_{o0}$, intermediate radius $AC = r_{i0}$ and core radius $AB = r_{ii}$. Core radius r_{i0} of the outer tubule is set equal to the outer radius of the inserted scroll. (b) Upper half of the bent tubule (bead). $OD' = R_{o0}$, $OC' = R_{i0}$ and $OB' = R_{ii}$ denote radii with common centre O . The structure of course still has a cylindrical symmetry about the axis of the tubule, represented by thick dark line. $OA = a$ is the axial offset, and $\rho_m = AD'$.

6 Structure of tubules and beads

Fig. 3a (water-glycerol 80-20 v/v solvent) shows a tubule with a bead. The part of the tube with uniform cross-section la-

belled I (referred to as (3-I)) consists of a single tubule ($k=1$) (fig. 3b) and is reasonably symmetric in the two halves. The scaling parameter $\alpha = 0.46$. Cross-section labelled II (3-II) corresponds to the widest part of the bead. As can be seen in Fig. 3a, this part has an *additional patch*; indeed the best fit for (3-II) requires two values of k , i.e., two separate tubules (fig. 3c). Note that α for (3-II) is 1.3 times that for (3-I). A higher value of α for (3-II) reflects a lower number density of the dye molecules, as compared to that for (3-I). For the bead shown in fig. 4a (water-glycerol 10-90 v/v solvent), the parameter α is again found to be larger for the bulged part (fig. 4(b),(c)), compared to that for the straight part. Fig. 5a (water-glycerol 10-90 v/v solvent) shows a tubule having additional lamellae wrapped *outside* the main tubule. Analysis of (5-I) shows that it consists of 2 tubules (fig. 5b). Cross-section (5-II) consists of 3 tubules (fig. 5c); a solvent gap exists between the main tubule and the outer tubule. Analysis of (5-III) shows that it comprises 4 tubules (fig. 5d). The α values are *similar* in all sections analysed. Thus, a higher value of α is found for the bent-part compared to the straight part.

7 Phenomenological model for beads

The *syringe-coated* sample cells are likely to have a non-uniform spreading of lipid compared to the spin-coated samples, which upon drying will contain numerous holes and edges in the lamellar stack. Upon swelling (fig. 2a,b), it could be that some of the lamellar patches which do not extend over the entire area of the sample form edge dislocation loops. Such a patch, lying on top of the outermost bilayer of a growing tubule is likely to attach itself to the exterior of the tubule (fig. 5a). A patch below the layers forming the wall of the growing tubule, and located sufficiently close to its root could get entrained into the solvent core because of fluid flow (fig. 7a). The curvature energy of the entrapped lamellar structure (which could be a vesicle or a scrolled structure) can get reduced if it expands in diameter, in turn pushing the wall of the tubule radially outward and producing a bulge (fig. 7b). This broad picture is consistent with the observation that beads have additional layers inside the bulging region (fig. 2c, fig.3a, fig.4a) and bulging is not observed if additional lamella are outside the main tubule (fig. 5a).

A full calculation of the equilibrium shape of the bead requires minimisation of the total energy, which includes curvature and dilation energies at the neck regions, apart from membrane tension. We do not address this complex problem, but investigate the feasibility of the mechanism outlined above by developing a highly simplified model described below. We model inserted lamella patch as a cylindrically symmetric structure with fixed lamellar spacing (which could be a scroll with open ends merging into nearby layers, or a closed vesicle). We assume that the layer spacing is fixed at the equi-

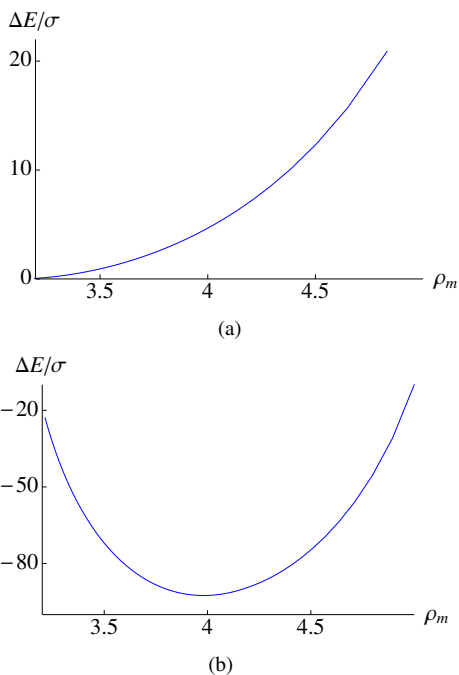


Fig. 8 Change in energy ($\Delta E/\sigma$) ($\times 10^{-11} \text{ m}^2$) as a function of $\rho_m = (R_{oo} - a)$ (μm), (a) straight configuration of fig. 7a. (b) Beaded structure of fig. 7b. ($\Delta E/\sigma$) < 0 and is minimum at $\rho_m \simeq 4 \mu\text{m}$. $r_{oo} = 3.15 \mu\text{m}$, $r_{io} = 2.3 \mu\text{m}$, $r_{ii} = 0.1 \mu\text{m}$, $L_i = 9 \mu\text{m}$, $\kappa/\sigma = 20 \mu\text{m}$. $L_o = 9 \mu\text{m}$ for (a).

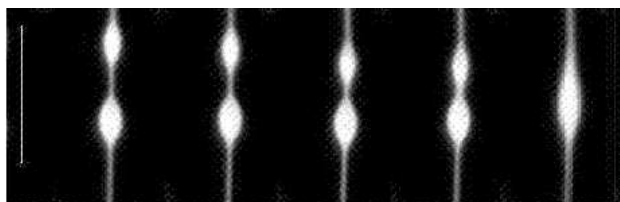


Fig. 9 Approach and coalescence of beads, scale bar $20 \mu\text{m}$. Till coalescence, the inter-bead separation fits $d(\mu\text{m}) = 6.6 - 0.6t$ (s).

librium value, as in many other problems involving smectic liquid crystals¹⁶. This dictates that the inner and outer tubules bend with a circular cross-section in the plane containing the tubular axis, about a common centre O, which is shifted away from the tubule axis (fig. 7b). We ignore the excess energy of the conical edge of the outer tubule (the region near the neck of the bulge) for simplicity. In what follows, we use the conventional cylindrical co-ordinate system (ρ, ϕ, z) with its origin at A, and z -axis along the tubule axis (fig. 7), rather than the one used in fig. 6.

We now calculate the energies of the two configurations of fig. 7. The total bend angle is 2θ . The volume of the inner cylinder before bending is $V_{ic} = \pi(r_{io}^2 - r_{ii}^2)L_i$. After bending (fig. 7b), the volume of the bent inner patch is given by $V_{ib} = 2 \int_0^{2\pi} d\phi \left(\int_{z_1}^{z_2} dz \int_{\rho_1}^{\rho_2} \rho d\rho + \int_{z_3}^{z_4} dz \int_{\rho_3}^{\rho_4} \rho d\rho \right)$, where the limits of integration are $z_1 = 0$, $z_2 = R_i \sin \theta$, $\rho_1 = (R_i^2 - z^2)^{1/2} - a$, $\rho_2 = (R_o^2 - z^2)^{1/2} - a$, and $z_3 = R_i \sin \theta$, $z_4 = R_o \sin \theta$, $\rho_3 = z \cot \theta - a$, $\rho_4 = (R_o^2 - z^2)^{1/2} - a$. This simplifies to $V_{ib} = 2\pi[(2/3)(R_{io}^3 - R_{ii}^3) \sin \theta - (R_{io} \cos \theta - r_{io})(R_{io}^2 - R_{ii}^2)\theta]$. Since $(R_{io} - R_{ii}) = (r_{io} - r_{ii})$, for any given R_{ii} the angle θ is fixed to ensure that $V_{ib} = V_{ic}$. As θ is the same for the bent outer tube, the corresponding volume V_{ob} is obtained by replacing R_{io} and R_{ii} by R_{oo} and R_{io} respectively in the above expression. The equivalent volume before bending is $V_{oc} = \pi(r_{oo}^2 - r_{oi}^2)L_o$, where L_o is the length needed to ensure $V_{oc} = V_{ob}$. The bent part of the outer tubule can of course draw material from the long tubule, and usually $L_o > L_i$. The curvature elastic energy E_c is calculated by integrating the energy density $(K_1/2)(\nabla \cdot \mathbf{n})^2$, (where \mathbf{n} is the director) over the relevant volume¹⁶. For the straight configuration

$$E_c = \pi K_1 [L_i \ln(r_{io}/r_{ii}) + L_o \ln(r_{oo}/r_{io})]. \quad (3)$$

Since the curvature energy E_b in the bent configuration does not reduce to a simple expression, we evaluate it numerically. The surface area of the cylinder with total volume ($V_{oc} + V_{ic}$) exposed to the surrounding liquid changes after bending, even though the volume is conserved. The total exposed area of the straight configuration is

$$A_c = 2\pi[r_{ii}L_i + (r_{io}^2 - r_{ii}^2) + r_{oo}L_o + r_{io}(L_o - L_i)]. \quad (4)$$

The corresponding energy is σA_c , and σ is used for the two ends of the inner cylinder also. After bending, a calculation similar to the one for V_{ib} (see above) for the exposed area leads to

$$A_b = 4\pi[(R_{ii}^2 + R_{oo}^2) \sin \theta - a \theta (R_{ii} + R_{oo}) + (R_{io} - R_{ii})((1/2)(R_{ii} + R_{io}) \cos \theta - a)], \quad (5)$$

where $a = OA = (R_{io} \cos \theta - r_{io})$ (fig. 7b).

We can now calculate the total energy ($E_b + \sigma A_b$) and compare it with the corresponding value ($E_c + \sigma A_c$) of equivalent volumes of both the inner and outer cylinders. We have

used layer spacing $d \simeq 6$ nm, bending rigidity¹⁷ $K_1 \simeq 10$ pN, membrane tension¹⁸ $\sigma \simeq 5 \times 10^{-7}$ N/m (*i.e.*, the length scale $K_1/\sigma \simeq 20\mu\text{m}$). The structure bulges only if the total energy is reduced and the difference ΔE is negative. We vary the initially assumed R_{ii} to find the absolute minimum of energy, corresponding to the equilibrium structure. Illustrative energy curves are shown in fig.8 as a function of $(R_{oo} - a)$ ($> r_{oo}$), which is the physically measured maximum radius of the bead. It is clear that in the absence of the inner tubule, the outer tubule remains straight, whereas inclusion of the inner tubule leads to bead formation, mainly to lower the curvature energy. For tubules with two beads, calculations show that the energy is lowered by their merger. Such a bead coalescence is actually observed in experiments (fig.9), and corroborates the proposed mechanism based upon curvature elasticity. When additional material wraps on the outer surface of an existing tubule (as in fig.5), there is obviously no gain in energy by bulging of the tubule, which remains straight.

8 Conclusions

We have described the formation of complex, nested topologies of a common well-hydrated phospholipid in the L_α phase. Specifically, we find that introduction of water to a dry mass of lipid by capillary action gives rise to an abrupt burst event characterised by rapid appearance of microscopic tubules, which trigger the formation of long-lived additional new multilamellar tubules. In these post-burst, long-lived tubules an unusual complex topography appears reproducibly. Specifically, we observe localised bulging of some tubules (bead formation) in which additional lamellar inclusions are found within the tubule interior. We also observe tubules with exterior lamellar attachments. We have used FCPM to analyse the structure of tubules observed. We have suggested a mechanism for addition of lamellar material inside the tubules, and argue that the overall energy can be lowered by bead formation when a sufficiently large lamellar patch gets inserted in the solvent core of the tubular structure. These protrusions, which grow from the lipid-water interface are remarkable structures, tens of micrometer wide. Because myelins grow as a consequence of kinetics of hydration, it appears reasonable that differences in methods of hydration may also stabilise complex tertiary self-assemblies leading to unusual, nested topologies.

9 Acknowledgement

We acknowledge A. A. Deshpande for his help in image processing. TB acknowledges John H. Ipsen and Atul N. Parikh for very helpful discussions.

References

- 1 R. Virchow, *Virchows Arch.*, 1854, **6**, 562.
- 2 D. Chapman and D. J. Fluck, *J. Cell Biol.*, 1966, **30**, 1.
- 3 H. Sandermann, H. Falk and G. Schumacher, *Analytical Biochemistry*, 1977, **82**, 583–585.
- 4 I. Sakurai, T. Suzuki and S. Sakurai, *Biochimica et Biophysica Acta*, 1989, **985**, 101.
- 5 L. N. Zou and S. R. Nagel, *Phys. Rev. Lett.*, 2006, **96**, 138301.
- 6 L. N. Zou, *Phys. Rev. E.*, 2009, **79**, 061502.
- 7 J. R. Huang, L. N. Zou and T. A. Witten, *Eur. Phys. J. E.*, 2005, **18**, 279.
- 8 L. M. G. Vangolde, J. J. Batenburg and B. Robertson, *Physiological Reviews*, 1988, **68**, 374–455.
- 9 E. Evans, H. Bowman, A. Leung, D. Needham and D. Tirrell, *Science*, 1996, **273**, 933–935.
- 10 A. Karlsson, R. Karlsson, M. Karlsson, A. S. Cans, A. Stromberg, F. Ryttsen and O. Orwar, *Nature*, 2001, **409**, 150–152.
- 11 L. A. Bagatolli and E. Gratton, *Biophysical Journal*, 2000, **78**, 290.
- 12 R. Gomati, M. Gharbia and A. Gharbi, *Optics Communications*, 1994, **111**, 71.
- 13 L. B. A. Johansson, *Biochimica et Biophysica Acta*, 1993, **1149**, 285.
- 14 T. Bhatia, *To be submitted*.
- 15 P. R. Bevington and D. K. Robinson, *Data Reduction and Error Analysis for the Physical Sciences*, McGraw-Hill, Boston, 2002.
- 16 P. G. de Gennes and J. Prost, *The Physics of Liquid Crystals*, Oxford University Press, Oxford, 1994.
- 17 J. Pan, S. Trisham-Nagle and J. F. Nagle, *Biophysical Journal*, 2008, **94**, 117–124.
- 18 J. R. Henriksen and J. H. Ipsen, *Eur. Phys. J. E*, 2004, **149**, 149–167.

Our fluorescence microscopic studies reveal that multilamellar tubules growing on hydration of lipids often entrain lamellar patches, resulting in the formation of isolated beads. We develop appropriate models that enable a quantitative description of these structures, and use elasticity theory to account for their stability.

